Research article

Blue-LED assisted Photodegradation kinetics of rhodamine-6G dye, enhanced anticancer activity and cleavage of plasmids using Au-ZnO nanocomposite

Pilavadi Thangamuniyandi [a], Devan Umapathy [b], Loganathan Nagarajan [a,c,*], Antony Joseph Velanganni Arockiam [b]

[a] School of Chemistry, Structural and Photochemistry Laboratory, Bharathidasan University, Tiruchirappalli, 620 024, Tamil Nadu, India
[b] School of Life Sciences, Department of Biochemistry, Molecular Oncology Laboratory, Bharathidasan University, Tiruchirappalli, 620 024, Tamil Nadu, India
[c] UGC Faculty Recharge Programme, UGC, New Delhi, India

ARTICLE INFO

ABSTRACT

The plasmonic metal doping on the UV-active metal oxide nanoparticle turns the resultant plasmonic metal-metal oxide (PMMO) into visible light active and upon exogenous illumination the photogenerated energetic charge carriers and the *in situ* generated reactive oxygen species (ROS, e.g. $\cdot OH$ and O_2^-) authoritatively enhances its biological and catalytic activity. Herein, a hexagonal rod-shaped ZnO nanoparticles (NP) precursor was prepared using the sol-gel method, which in the presence of varying concentrations of gold (0.005M, 0.01M, and 0.015M) *via* a greener citrate reduction method afforded a nanocrystalline Au-ZnO nanocomposite. Using which, the visible-light driven photo-degradation kinetics investigation of rhodamine-6G (R6G) dye under blue LED irradiation were carried out. The use of 20 mg 0.015-Au-ZnO completes the degradation of R6G (97.0 %, k = 6.5 X $10^{-3}s^{-1}$ at pH 7) within 55 min while 50 mg of 0.015-Au-ZnO catalyst improves the rate of R6G degradation (15 min 97.8 %, k = 14.8×10^{-3} s^{-1}) and it is reusable up to three cycles. The LC-MS spectra of the remains of R6G (after 15 min) identified various low molecular ions (up $m/z = 65$). Further, the blue-LED assisted anti-cancer studies (MTT assay) using 0.015-Au-ZnO towards human lung cancer cells (A549), breast cancer cells (SKBr3) show high anti-proliferation rate and low cytotoxicity against healthy human embryonic kidney cells (HEK-293) with an IC$_{50}$ value of 65, 53 and 124 μg/mL respectively. Also, the AO-EB dual staining and DCFH-DA analysis of SKBr3 and A549 cells revealed ROS-mediated cell death *via* apoptosis. Moreover, plasmid cleavage studies against supercoiled pBR322 DNA result in single-stranded linear DNA without traversing the nicked circular form, suggesting the possible DNA targeting activity of Au-ZnO nanozyme. Thus, the synthesized Au-ZnO nanocomposite shows excellent photocatalytic and biological activity.

* Corresponding author. School of Chemistry, Structural and photochemistry Laboratory, Bharathidasan University, Tiruchirappalli, 620 024, Tamil Nadu, India.
E-mail address: l.nagarajan@bdu.ac.in (L. Nagarajan).

1. Introduction

Water is an elixir of life, however, in the name of industrialization and urbanization, water resources and potable nature are being destroyed [1]. Access to clean water is a cornerstone of a healthy economy; according to the WHO and UNICEF 2022 report, 25 per cent of the world's population has no access to safe drinking water [2,3]. Hence, water treatment becomes vital to retrieve its potability and the advanced oxidation process (AOP) is one of the promising methods developed for the same [4–12]. It involves the *in-situ* generation of reactive oxygen species (ROS) such as •OH and O_2^- radicals etc., through various external stimuli [9–12]. Photochemical AOP (PAOP) is the long-established decontamination protocol, in which the use of semiconductor photocatalysts such as titania (TiO_2) and zinc oxide (ZnO) results in a complete breakdown of organic pollutants without any secondary pollutants generation and lead to mineralization [13–17]. Incidentally, both ZnO and TiO_2 are UV active because of their wider band gap (~3.2–3.3 eV) and the band gap engineering with the help of plasmonic metals (e.g. Ag, Au) makes it visible light responsive material [16,17]. This may be due to two reasons, one, the creation of the Schottky barrier height at the junction of plasmonic metal-metal oxide (PMMO) enhances the charge separation and in turn, restricts the electron-hole recombination [18,19], two the local surface plasmon resonance effect (LSPR) of the plasmonic metal facilitates hot electron injection to semiconductor conduction band [16–23]. Further insight into this matter reveals that the LSPR effect has a multifold role to play in the enhancement of photocatalysis namely: it extends the spectral absorption range towards the visible region, augments the local electromagnetic field and concurrently produces the photothermal heating effect. The stronger the electromagnetic field, the greater the separation of photogenerated electron-hole pairs and drastically reduces the rate of recombination [21]. Chen et al. with the help of a heat transfer model demonstrated that the temperature of AuNP tremendously increased to 795K under the reaction conditions [22]. Linic and coworkers showed that the oxidation rate of photothermal catalysis is multifold times higher than the photocatalysis (mol h^{-1}g^{-1} and µmol h^{-1}g^{-1} respectively) owing to the LSPR effect [23]. Thus, a library of PMMOs was developed for numerous high-profile applications such as environmental remediation in the form of industrial effluent treatment, water purification, water splitting, solar energy conversion, nano-drug carriers, etc [5–25]. In particular, the use of PMMO in environmental remediation provides a holistic approach to mineralize the large number of industrial effluents that are otherwise resistant to chemical and biological processes [13,14,25].

Herein, Au-ZnO nanocomposite (NC) with varying concentrations of gold (0.005M, 0.01M, and 0.015M labelled as 0.005-Au-ZnO,0.01-Au-ZnO and 0.015-Au-ZnO respectively) were synthesized *via* the benign citrate reduction method and structurally characterized using powder-XRD, FESEM, HRTEM, EDS, UV–Vis-DRS and XPS analysis. The PXRD pattern of ZnO reveals a hexagonal wurtzite-type structure, and FESEM analysis confirms the same. Further, the PXRD patterns of all three Au-ZnO are similar with a weaker peak at 38.3° indicating the presence of Au (111 plane) [26,27]. The TEM analysis of Au-ZnO identified the randomly distributed spherical gold nanoparticles (AuNP) on a micrometer-long wire-shaped ZnO, the XPS analysis reveals the presence of both Zn2p/3p and Au4f peaks. As Au-ZnO's are visible-light active, photocatalytic activity towards industrial dye degradation such as rhodamine-6G dye (R6G) was carried out using blue-LED (λ~455 nm) irradiation. Earlier, 3.0 wt% of Au-doped ZnO synthesized *via* microwave synthesis completed the R6G degradation with a much slower rate (k = 1.62 × 10^{-3} min^{-1} corresponds to 2.7 × 10^{-5} sec^{-1}) [28]. In the present study, a complete degradation of R6G was achieved (97 %) using 50 mg of 0.015-Au-ZnO within 15 min and at a much higher rate (k = 14.8 X 10^{-3}s^{-1}). Also, the colorimetric analysis using 50 mg of 0.015-Au-ZnO observed a dramatic colour change from red-orange to colourless within 15 min.

Phototheranostics is an emerging and adjuvant treatment for cancer that provides synergistic antitumour efficacy by encompassing a combinatorial therapeutic modality such as photodynamic (PDT) and plasmonic photothermal therapy (PTT). Herein, the plasmonic noble metal nanoparticles with PDT/PTT agents unveil enhanced optical absorption properties owing to their LSPR effect [29–32]. Both ZnO and Au are biologically active and are widely used in many biological applications [33–36]. It is found that the AuNPs show excellent photothermal response with minimum side effects, and particularly the photothermal heating effect significantly increases with the size of AuNPs. Also, AuNPs efficiently generates ROS species such as hydroxyl and superoxide radicals under ambient conditions [32,33]. In other words, to enhance their efficacy, exogenous illumination is essential, which boosts the light-to-heat conversion and effectively generates a significant amount of intracellular ROS. These ROS become an effective antagonist for malignant cells and pave the way for ROS-based nanomedicine [34–39]. Thus, the MTT assay under blue-LED irradiation of ZnO and Au-ZnO (0.005-Au-ZnO, 0.01-Au-ZnO, and 0.015-Au-ZnO) was investigated. The 0.015-Au-ZnO nanocomposite was more effective against the breast cancer cell line (SkBr3 IC$_{50}$ = 53 ± 1.02 µg/ml) than the lung cancer cell line (A549, IC$_{50}$ = 65 ± 1.02 µg/ml), and exhibits relatively low cytotoxicity towards healthy human embryonic kidney cell lines (HEK-293, IC$_{50}$ = 124 ± 1.02 µg/ml). The acridine orange-ethidium bromide (AO-EB) dual staining method shows the presence of more orange-stained irregularly shaped cells revealing the apoptotic pathway of cancer cell death mechanism and the use of DCFH-DA assay further strengthens the observation by quantifying the endogenous ROS generation [40–43]. It is to be noted that the accumulation of ROS molecules in cancer cell cytoplasm provokes apoptotic pathways which cause mitochondrial membrane potential (MMP) loss. Also, the excess ROS leads to severe oxidative damage and cell membrane rupture [44]. The DNA cleavage ability against pBR322 DNA under blue LED illumination shows that the super-coiled DNA (form I) was denatured and completely stranded to a linear form III without passing through the nicked circular form II. This also suggests that Au-ZnO is an efficient nanozyme and may act as a DNA-targeting anti-cancer drug.

2. Results and discussion

2.1. Synthesis and Morphological studies of ZnO and Au-ZnO

Herein, a greener wet chemical method was successfully attempted for the synthesis of both ZnO and Au-ZnO (see supporting

information) [45,46]. The ZnO was calcined at 400 °C for 3hr to obtain off-white ZnO solid which was then treated with aqueous HAuCl$_4$ (0.005, 0.01 and 0.015 M) and sodium citrate solution under high temperature (180 °C for 48 h) in a Teflon lined stainless steel autoclave followed by calcination at 400 °C for 3 h. The original off-white ZnO was turned to dark gray, indicating the formation of Au-ZnO. Here in, sodium citrate not only acting as reducing agent but also as a capping agent for Au-ZnO. Also, the calcination on or above 400 °C improves the crystallinity, which in turn the photocatalytic activity of the Au-ZnO nanocomposite. The formation of hexagonal rod-shaped ZnO nanostructures in various sizes ranging from 300 to 400 nm is evident from FESEM analysis (Fig. 1A). Fig. 1B–D shows the TEM micrograph of 0.005, 0.01, and 0.015-Au-ZnO respectively, in which the presence of micrometer length ZnO wires are clearly visible over which the Au NP's are distributed as microdots. In other words, the addition of AuNP over ZnO forms AuNP decorated ZnO wires. Further, the energy-dispersive X-ray analysis (EDX) of ZnO and Au-ZnO confirms the composition of Zn, O, and Au in the respective nanostructures and shows that the 0.015-Au-ZnO contains only 0.8 wt % of Au in the ZnO matrix, (Fig. 1E–F).

2.2. X-ray photoelectron spectroscopic (XPS) analysis

XPS investigation reveals the composition and valence state of the given elemental surface. Fig. 2A represents the XPS survey spectra of ZnO and Au-ZnO which ascertain the presence of Au, Zn, O, and C elements with no other impurities. All the peaks were
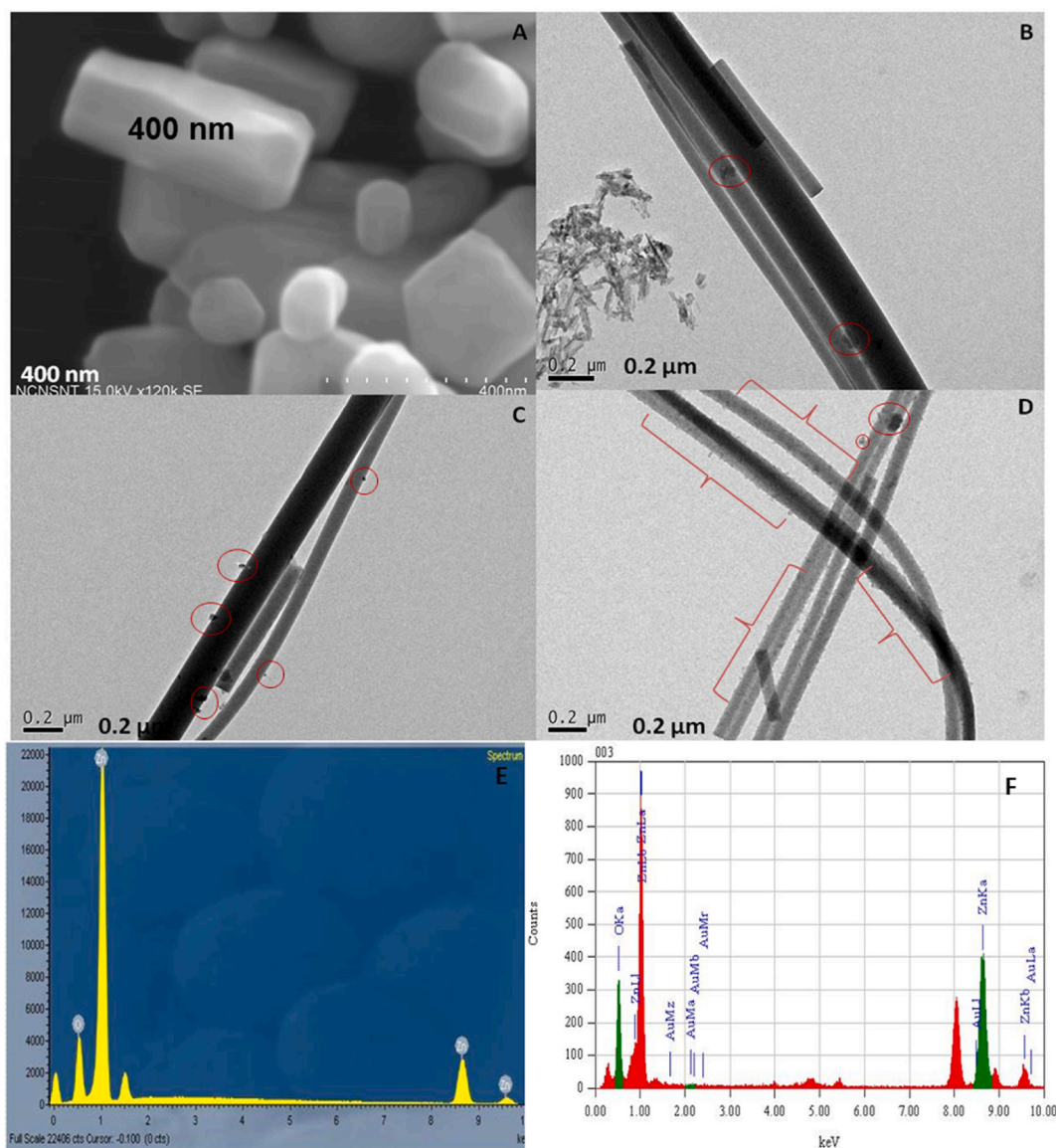

Fig. 1. (A) FESEM image of ZnO; (B)–(D) TEM images: (B) 0.005-Au-ZnO; (C) 0.01-Au-ZnO; (D) 0.015-Au-ZnO; (E) FESEM-EDX spectra of ZnO NP; (F) TEM-EDS spectra of Au-ZnO NC (showing 0.8 wt% of Au). The red cricles and lines indicating the presence of Au NP's.
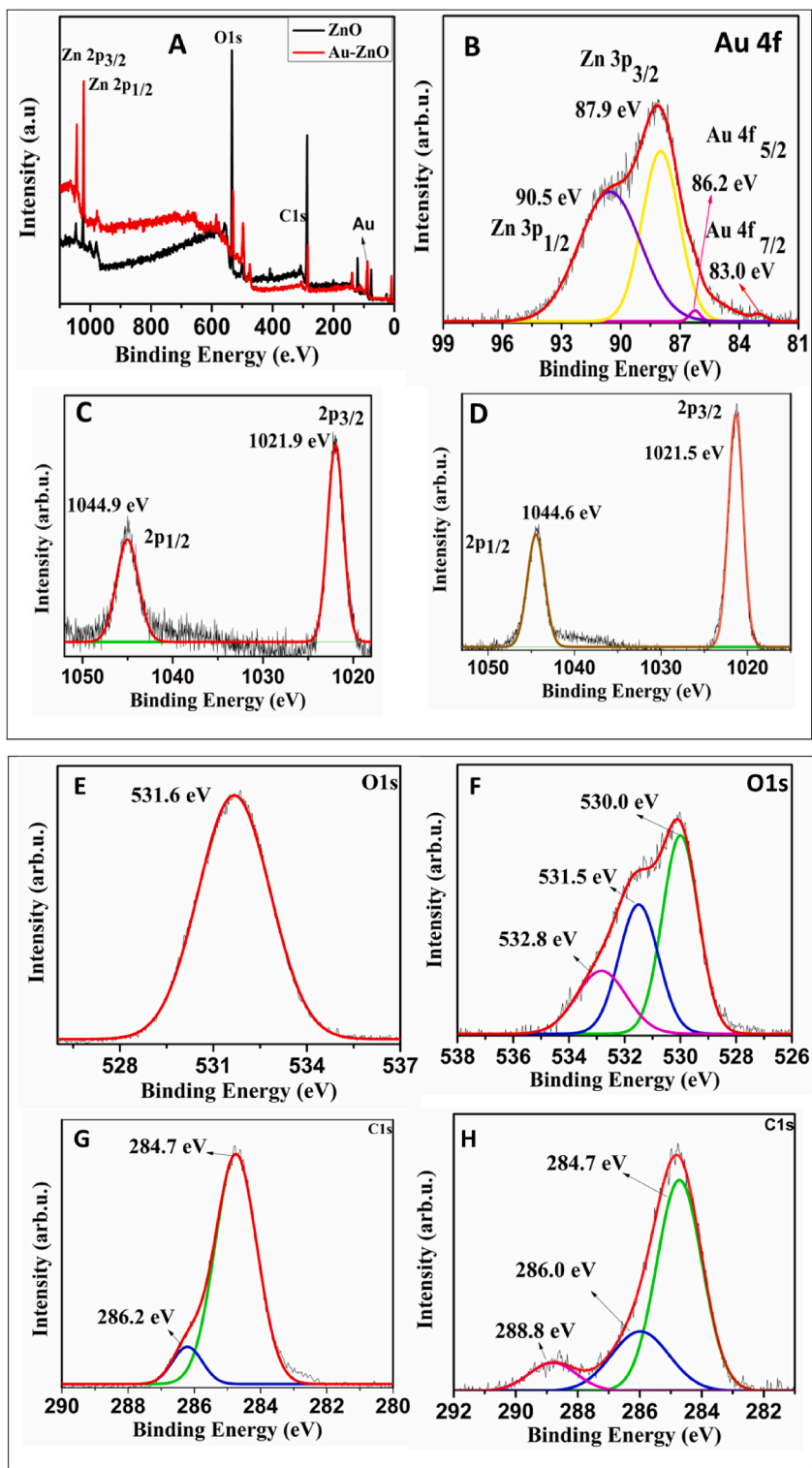
Fig. 2. XPS spectra of ZnO and Au-ZnO (A) Survey spectrum; (B) Au 4f; (C) Zn 2p of ZnO (D) Zn 2p of Au-ZnO (E) O1s of ZnO; (F) O1s of Au-ZnO; (G) C1s of ZnO; (H) C1s of Au-ZnO.

assigned with reference to binding energy (BE) of adventitious C1s peak at 284.7 eV (Fig. 2G–H). It is a well-known fact that the Zn3p overlap with Au 4f, and it is quite evident from the Au 4f spectra (Fig. 2B) of Au-ZnO, which contain both Au 4f ($4f_{7/2}$ @ 83.0 and $4f_{5/2}$ @ 86.2 eV) and Zn3p peaks ($3p_{3/2}$ @ 87.9 and $3p_{1/2}$ @ 90.5 eV) in accordance with the earlier reports [26–28,47–53]. Also, the high-resolution Zn2p XPS spectra of pristine ZnO (Fig. 2C) show a characteristic doublet located at 1044.9 and 1021.9 (corresponding to $Zn2p_{1/2}$ and $Zn2p_{3/2}$) with an expected energy separation of (ΔBE) 23 eV while the doublet in Au-ZnO appeared at 1044.6 and 1021.5 eV which is slightly lower than the pristine ZnO (Fig. 2D). Thus, the significant shift of Au4f (by 1.0 eV against the bulk gold 84.0 eV) and Zn2p indicating the strong metal support interaction (SMSI) exist between the ZnO support and the AuNP. Earlier, Casaletto et al. [54] found that the BE of Au^+ and Au^{3+} species supported on TiO_2, SiO_2 and CeO_2 appears at $Au4f_{7/2}$ = 85.6–85.8 and 86.5 eV respectively along with Au^0 species at 83.9–84.5 eV, while Wolski et al. [55,56] reported the presence of $Au^{\delta-}$ species in Au-ZnO and Au-ZnNb$_2$O$_6$ nanocomposites in the region of 83.1 and 82.8–83.3 eV respectively. Further, it is suggested that the SMSI causes the electron transfer from ZnO to Au and in turn the metallic AuNP's acquires partial negative charge to form a $\{Au^0\}^{\delta-}$ species [55–57]. In the present case, the negative offset on the BE of Au4f confirming the presence of $\{Au^0\}^{\delta-}$ species.

The symmetric O1s spectra of ZnO (Fig. 2E) indicate their high purity and centred at 531.6 eV, while in Au-ZnO two deconvoluted peaks at 532.8 and 530.0 eV may be assigned as oxygen-containing surface species and the lattice oxygen respectively [26–28,50–53]. Recently, Frankcombe et al. explained that the O1s peak around 531 eV (here in 531.5 eV) was not due to an oxygen vacancy site or oxygen-deficient region but the O1s electrons of a chemisorbed water molecule [58]. Also, the C1s spectra of Au-ZnO (Fig. 2H) consist of three deconvoluted peaks that may be assigned to C-C (284.7 eV) and carboxylate carbonyl units of citrate in Au-ZnO (C-C=O 286.0 eV and C=O 288.8 eV) while in ZnO the small fractions of C1s at 286.2 eV may be derived from the oxalic acid that was used during the synthesis of ZnO.

2.3. Powder XRD analysis

The crystallinity, purity, and phase of the sample were identified using PXRD analysis. Fig. 3 shows the PXRD pattern of prepared ZnO and Au-ZnO (0.005, 0.01, and 0.015 M). It consists of various peaks at 2θ = 32.0°, 34.6°, 36.5°,47.7°, 56.7°, 63.0°, 66.60, 68.20, and 69.2° may be indexed to (100), (002), (101),(102), (110), (103), (200), (112) and (201) crystal planes respectively of hexagonal wurtzite ZnO structure (JCPDS card No.36-1451) [59]. The PXRD patterns of all four samples are sharp and intense, suggesting the high crystalline nature of the samples. Particularly, the 100, 002, and 101 phases are dominant, indicating that these phases determine the properties of the resultant nanocomposites. Also, all four XRD patterns are similar and no characteristic gold peaks are present. This rules out the substitution of Au on the ZnO crystalline lattice and supplements the HRTEM observations. However, the magnification of the PXRD spectra (inset of Fig. 3) shows a small peak at 38.3° may be indexed as (111) plane of Au (JSPDS card no (04–0784) [26,27, 59]. The lower gold doping and the presence of sodium citrate capping agent as evident from the C1s asymmetric XPS spectra (Fig. 2H) may be the reasons for the hidden nature of gold planes.

2.4. Electronic properties

It is possible to fine-tune the functional properties of semiconductor nanomaterials just by modifying the number and nature of the defect sites. In other words, the band gap engineering of ZnO disturbs the zinc-to-oxygen ratio either by introducing a deeper oxygen defect or by causing shallow zinc atoms to interstitial with oxide atoms [56,59,61]. Essentially, ZnO is an n-type semiconductor with a band gap energy (E_g) of 3.37 eV, and the defect-rich ZnO as obtained from the thermolytic method $\geq$250 °C, shifts the absorption edge
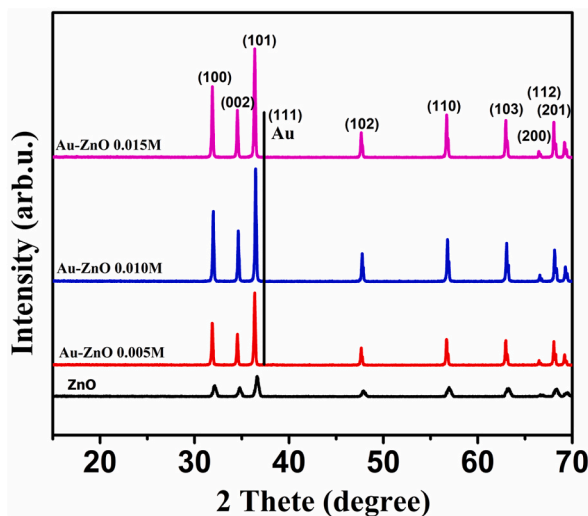

Fig. 3. Powder XRD patterns of (a) pure ZnO; (b) 0.005-Au-ZnO; (c) 0.01-Au-ZnO; (d) 0.015-Au-ZnO.

close to 3.2–3.3 eV [59]. Earlier, Driess and co workers demonstrated that the thermal treatment of ZnO between 150 and 800 °C tremendously reduces the bandgap to 3.40–2.95 eV [60]. The UV–visible-diffuse reflectance spectroscopic analysis (UV–Vis-DRS) of ZnO and Au-ZnO shows a characteristic band edge absorption occurs at 365 nm for ZnO (corresponds to the electron transition of valence band to conduction band of ZnO). Additionally, Au-ZnO contains typical LSPR absorption in the visible region of 530–550 nm (λ_{max} 536 nm for 0.005-Au-ZnO; λ_{max} 539 nm for 0.01-Au-ZnO and λ_{max} 549 nm for 0.015-Au-ZnO as in Fig. 4). Further, in our case, as the ZnO and Au-ZnO were prepared by thermal treatment at 400 °C, the E_g of ZnO was shifted towards 3.20 eV and by doping with gold (0.015M), E_g was slightly reduced to 3.17 eV (Fig. S1). In general, the electronic properties of PMMO's are mainly depends on the concentration of the plasmonic metal and the annealing temperature. Apart from this, the size, morphology, and interparticle distances of metal nanoparticle will also affect the same [21,56]. In our case, the observed LSPR band is clearly red shifted from 536 nm to 549 nm with increasing the concentration from 0.005-Au-ZnO to 0.015-Au-ZnO. Owing to which, the mobility of the charge carriers at the surface were enormously increased and that facilitate the effective interaction with adsorbed O_2 and H_2O molecules to form the corresponding ROS species. This strong absorption clearly explains the enhanced photocatalytic activity of Au-ZnO under visible light illumination [16,17,23,50–52]. Moreover, the UV–Vis absorption of all the catalysts seems similar, inferring that the concentration of Au dopant is lower owing to which the band gap change is not much.

2.5. Photocatalytic activity

In general, dyes are bio-nondegradable and therefore severely inhibit the photosynthetic process and biota growth, which in turn increase chemical and biological oxygen demands. Thus, dye degradation becomes essential for the supply of pure and drinkable water. Our thorough literature analysis reveals that the reports on various industrial dye degradation are huge. However, the reports on the rhodamine 6G (R6G) is scarce. Herein, the photocatalytic activity of as-prepared Au-ZnO nanocomposites was demonstrated against rhodamine-6G dye (R6G) degradation studies. R6G dye is a fluorophore of the xanthene family and finds applications in dye lasers, printing, tracer dyes, etc. However, the effluent containing R6G is highly corrosive and carcinogenic and causes severe damage to rat retinal ganglion cells [62]. The UV–Vis spectra of R6G show three high energy absorbances at 256, 290 and 350 nm representing the π-π* & n-π* transition of the aromatic portion of R6G and a visible absorption at 527 nm corresponds to the charge-transfer transition [63].

Freshly prepared ZnO and Au-ZnO (0.005, 0.01, and 0.015M of Au) were used as photocatalysts for R6G dye degradation. The reaction was carried out in a cylindrical vessel and inside of which was wrapped with blue LED strip lights (Fig. S2, see supporting information). In a typical experiment, a stock solution of 500 mg/L of R6G (~1 mM) was prepared, and 10 mL of which was diluted to 100 mL (0.11 mg/mL) and added to the photocatalyst of varying amount (10–50 mg). The vessel containing the resultant suspension was kept in the dark for 30 min, after which it was irradiated with a blue LED strip with constant stirring. The reaction was monitored using UV–Vis absorption analysis by observing visible absorption at 527 nm, using 5 mL aliquots of R6G at regular intervals of time (Fig. 5 and Table 1). Also, the catalytic degradation was monitored *via* the colorimetric method using 50 mg of 0.015-Au-ZnO (Fig. 5E), where a visible colour change from red-orange to colourless was observed within 15 min. The UV–Vis analysis shows a huge decline in intensity from 1.5 to 0.03 arb.u (Fig. 5A) indicating the possible structural deformation. However, it may be confirmed that the core structure of R6G might be retained, as the UV–Vis pattern of R6G at t_0 and t_n (n = 15 min) look similar.

As pH plays a vital role in photocatalytic reactions, the effect of pH on R6G degradation was investigated under various pH ranges using 0.015-Au-ZnO for a prolonged period of time (400 min, Fig. 5B). The semi-log plot of a $\ln C_t/C_0$ vs time (C_t and C_0 refer to concentrations of the reactant at time t and zero reaction time respectively) shows enhanced activity in neutral pH conditions (pH = 7)
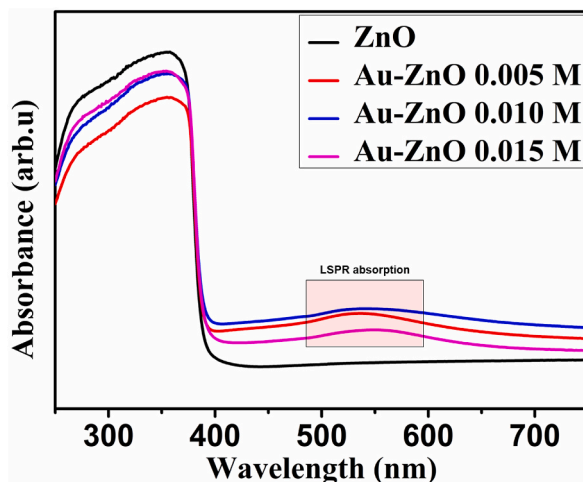

Fig. 4. UV–Vis-DRS spectra of ZnO (black), 0.005-Au-ZnO (red, LSPR@536 nm), 0.01-Au-ZnO (blue, LSPR@539 nm) and 0.015-Au-ZnO (magenta, LSPR@549 nm).
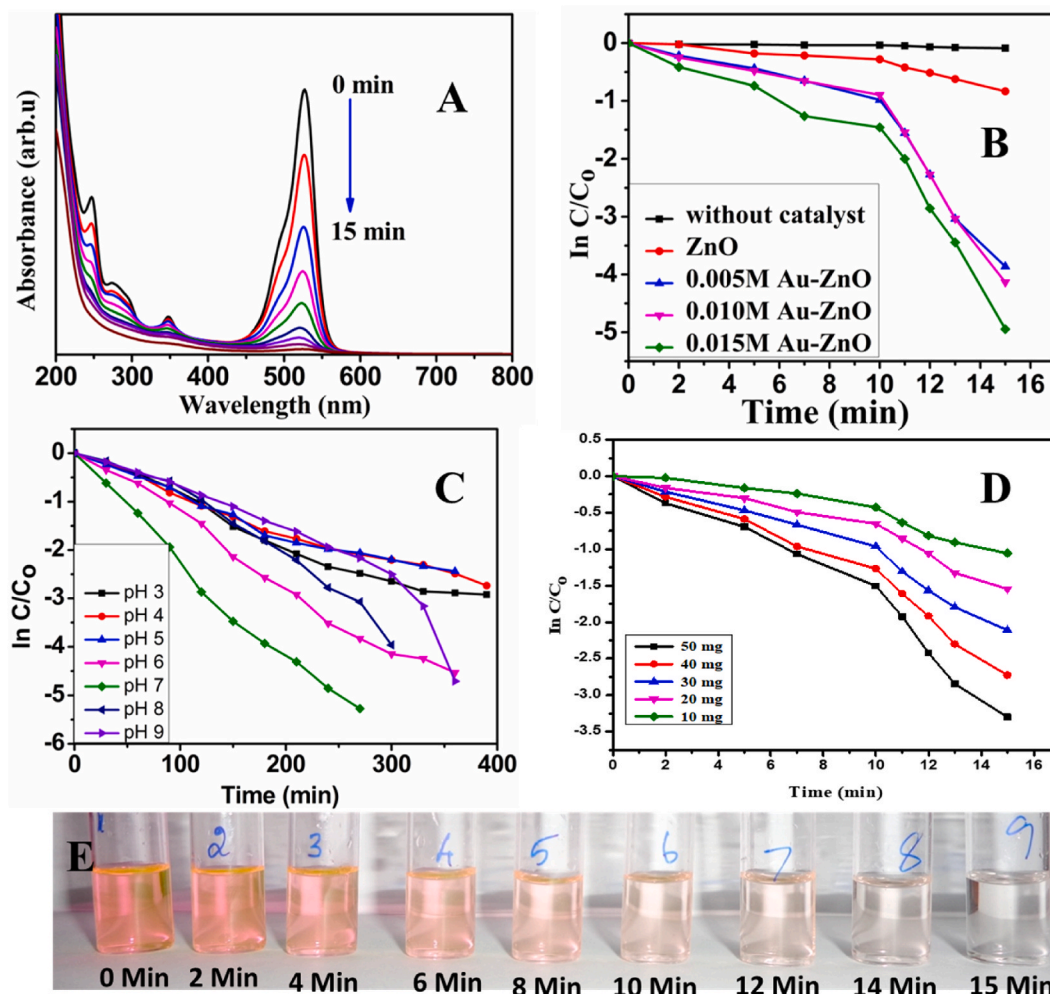
Fig. 5. (A) UV–Vis absorption profile of aqueous rhodamine 6G before and after degradaton by 0.015-Au-ZnO; kinetic plot (B) with 20 mg of ZnO and 0.005, 0.01 and 0.015 Au-ZnO catalysts (C) at various pH with 20 mg of 0.015-Au-ZnO; (D) effect of amount of Au-ZnO (E) Colorimetric observation of R6G with 50 mg of 0.015-Au-ZnO catalyst.

Table 1
Photocatalytic rhodamine-6G dye degradation studies at pH 7.0.

S.No	Name	Catalyst Weight	Time(min)	Slope	Rate Constant (Sec^{-1})
1	No Catalyst	–	75	−0.0052	0
2	ZnO	20	75	−0.0514	0.00085
3	0.005 M Au-ZnO	20	75	−0.2373	0.0039
4	0.010 M Au-ZnO	20	75	−0.2434	0.0040
5	0.015 M Au-ZnO	10	75	−0.2854	0.0047
6	0.015 M Au-ZnO	20	55	−0.3900	0.0065
7	0.015 M Au-ZnO	30	40	−0.5880	0.0098
8	0.015 M Au-ZnO	40	30	−0.6840	0.0114
9	0.015 M Au-ZnO	50	15	−0.8880	0.0148

and least activity in the pH range of 3–5, while pH 8 and 9 show intermediate activity close to neutral pH conditions. Thus, all photocatalytic reactions were carried out under neutral pH conditions. In general, heterogeneous photocatalytic dye degradations fit well with the Langmuir-Hinshelwood model which delineates the empirical relation between the initial concentration (on a logarithmic scale) of the compound and the observed reaction rate [10,17,28,33,34,53,56].

$$-\ln\frac{C_t}{C_0}=k_a t \ (\text{k}_a=\text{apparent rate constant}).$$

In all those cases, as the concentration of the dopant or the catalyst is significantly smaller, a pseudo-first-order kinetic equation is suitable, and accordingly, from the ln C_t/C_0 (or A_t/A_0) vs time plot (A_0, A_t are the absorbance at time 0 and t respectively) the rate of the reaction can be calculated by applying linear regression analysis (Table 1).

Fig. 5C shows the effect of Au doping concentration on ZnO with respect to the degree of degradation, and found that 0.015-Au-ZnO is highly effective. However, the plot reveals that the first 10 min of the reaction were relatively slower and completed the degradation process within the next 5 min of the reaction. This may be due to the *in situ* generated heat owing to the continuous illumination by blue LED strip light, in turn, reduces the volume of the reaction mixture and enhances the rate of the degradation process. The results of dye degradation are shown in Table 1. According to that, 20 mg of 0.005 and 0.01-Au-ZnO require 75 min to affect 80 % and 75 % of R6G degradation respectively, while 20 mg of 0.015-Au-ZnO causes 97 % degradation in 55 min. The use of 50 mg of 0.015-Au-ZnO results in a complete breakdown of R6G dye molecules (97.8 %, Table S3). The simple blue-LED irradiation shows no degradation, while ZnO (20 mg) is probably the slowest of all (10 % and k = 0.857×10^{-3} s^{-1}).

The variation in the amount of the catalyst and the concentration of the doping was examined (Fig. 5D). The observed rate is much greater for 0.015-Au-ZnO with 50 mg (14.8×10^{-3} s^{-1}) than 40 (11.4×10^{-3} s^{-1}) and 30 mg (9.8×10^{-3} s^{-1}) of the photocatalyst. Also, it is lower for 20 mg of 0.01 Au-ZnO (4.05×10^{-3} s^{-1}), 0.005 Au-ZnO (3.95×10^{-3} s^{-1}) which is still lesser than 10 mg of 0.015-Au-ZnO (4.6×10^{-3} s^{-1}) photocatalyst. The results from this study indicate that a higher concentration of Au doping, as well as a higher amount of catalyst, are necessary to affect the complete degradation of the R6G dye molecules. As the amount of the catalyst increases, the available active sites and ROS generation also increase, thereby increasing the rate of discolouration and dye degradation. The superior catalytic activity of the Au-ZnO nanocomposite may be due to the presence of the Schottky barrier and the resultant Fermi level equilibration (Chart 1). In other words, as the work function of ZnO (5.2 eV) is relatively higher than Au (5.0 eV), the transfer of electrons to ZnO occurs initially [19,20,61] and as the Fermi level energy of Au is higher than ZnO, it initiates the back transfer from Au and happens until it reaches equilibrium thereby creating a new Fermi level in the nanocomposite [19,20]. During visible light irradiation, equilibrated fermi-level electrons were injected rapidly into the ZnO conduction band *via* an LSPR mechanism. These injected electrons will now act as an efficient reducing agent and induce the formation of ROS radicals, which further mineralize the dye molecules (Chart 1) [20].

It was proposed that the enhanced photocatalytic activity of the Au-ZnO nanocomposite may be due to the *in situ* generated ROS species. These were awakened upon photo-irradiation from the adventitious oxygen molecule dissolved in the reaction medium. To confirm the *in situ* photogeneration of ROS in the reaction mixture, EPR spectra of the photocatalyst under the identical reaction condition as that of the photocatalytic experiment were recorded in water solvent using TEMPO (2,2,6,6-Tetramethylpiperidine 1-oxyl) reagent. It is well known fact that the EPR spectrum of solvated TEMPO shows a characteristic triplet pattern [34,35]. The idea is that the energetic electrons generated after photoirradiation of Au-ZnO NC were trapped with the help of TEMPO reagent, as this radical shows characteristic triplet EPR pattern of equal intensity (1:1:1), the addition of Au-ZnO without light illumination drastically reduced the intensity by 1.2 times while after the blue-LED illumination (20 min) maximise the intensity by 2.3 times (Fig. 6). The energised electrons react with the O_2 molecule and generates the $O_2^{-\cdot}$ which further helps to degrade the dye molecule [64]. Also, the triplet pattern is retained after the light illumination, suggesting the O_2 radical formation rather than the ·OH radical generation.
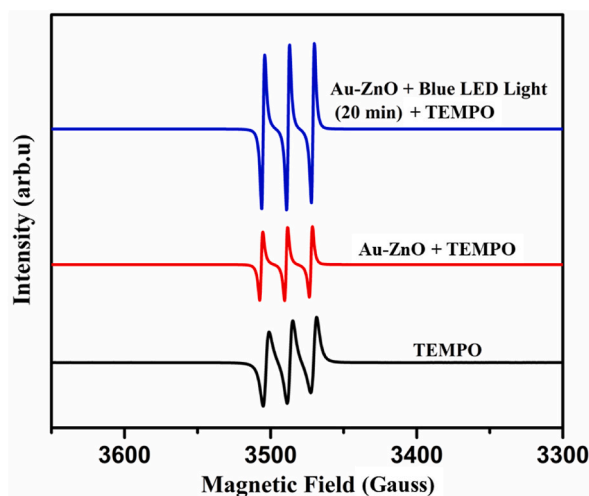

Fig. 6. EPR Spectra of 20 mM 2,2,6,6-Tetramethylpiperidine 1-oxyl(TEMPO) alone, with Au-ZnO and Au-ZnO with blue LED illumination for 20 min.

2.6. Stability and reusability of the Au-ZnO

The stability of the Au-ZnO was evaluated by irradiating an aqueous suspension of 0.005-Au-ZnO with blue LED light and sonicated for 1.5 h. The analysis of the resultant solution by UV–Vis-DRS analysis confirms that the Au-ZnO was quite stable (Fig. S3, see supporting information). The reusability of Au-ZnO was tested by centrifuging the catalyst from the R6G solution, washing it with deionized water, and drying it in an air oven at 100 °C. The re-used catalyst showed a successful response for the second and third cycles and showed similar photocatalytic behaviour against R6G degradation, which also illustrates that Au-ZnO nanocomposites can be reused for at least three cycles (Fig. S4 see supporting information).

2.7. LC-MS analysis of the photodegradation products

LC-MS spectrometric analysis determined the degradation products of R6G formed during visible light irradiation with 0.015-Au-ZnO (Fig. 7). Earlier, Tayade and Koodali groups individually identified fragmented ions of rhodamine B dye using ESI-MS analysis [65,66] while Rasheed et al. extended the observations to R6G dye molecular degradation [67]. On the basis of these previous reports, fragments of R6G ions are assigned. Accordingly, the initial photoexcitation of R6G in the presence of ZnO or Au-ZnO catalyst releases the ·OH radical which reacts with the acidic NH proton of R6G and forms the base peak at *m/z* 415. This corresponds to the loss of the ethyl group in the R6G molecule $[M - C_2H_5]$. The 7-min run of the LC-MS analysis shows several fragmented ions of lower molecular weight. Among these, the peaks at 387, 372, and 317 represent the loss of $-C_2H_5$, NH_3, and ethyl acetate molecules while the peaks at 249 and 231 correspond to the derivatives of phenylcyclopenta[b] chromenylium ions. It also contains lower molecular ion peaks at 113 and 65 may be assigned as the oxygen based radical as shown in Chart 1. Similarly, the recorded LC-MS spectrum after the completion of the photocatalytic reaction (15 min run) shows only two significant peaks at 114 and 74. Chart 2 summarizes the
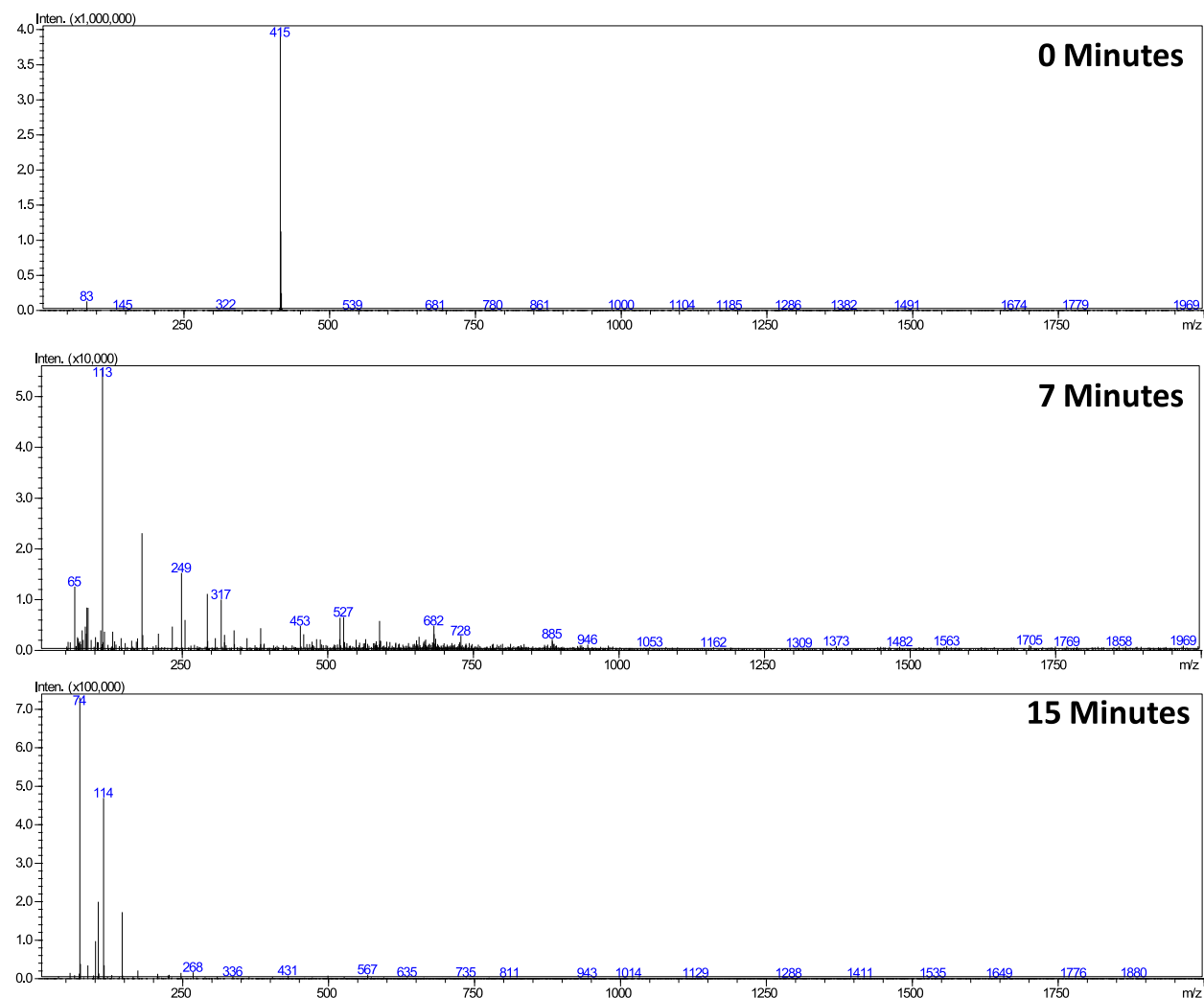

Fig. 7. LC-MS spectrum of Rhodamine 6G degradation products at (a) 0 min (b) 7 min (c) 15 min.

putative intermediates involved in the dye degradation process. The colorimetric analysis also confirmed that R6G dye completely breakdown within 15 min, and the LC-MS analysis complimented it very well.

2.8. Cytotoxic effect of ZnO and Au-ZnO nanocomposite

2.8.1. MTT assay

Several metal oxide nanoparticles exhibit antitumour activities against various malignant cells [39,68,69]. Among them, ZnO is most preferable owing to its unique properties [70–75]. MTT assay is a colorimetric assay widely used to determine viable cell numbers and the cytotoxicity [40,41]. Herein, the presence of a mitochondrial enzyme in metabolically active cells reduces the yellow tetrazolium salt of MTT (3-(4,5-dimethylthiozol-2-yl)-2,5-diphenyltetrazolium bromide) into a deep purple insoluble crystalline formazan product. After solubilization (mostly DMSO solvent), the spectrophotometric measurement reveals the number of viable cells, which is proportional to the amount of total formazan formed during the course of the reaction. Prior to the analysis, the photocatalysts were incubated for 24 h and irradiated with blue LED for 20 min. A 10–200 μg of catalysts were tested for 24 h screening against malignant lung cancer cells (A549), breast cancer cells (SkBr3), and healthy human embryonic kidney cells (HEK293), and the IC_{50} concentrations were calculated (Table 2). According to that, ZnO is least potent towards both the cancer cell lines (A549 174 ± 1.02, SkBr3 183 ± 1.08 μg/ml) while the 0.015-Au-ZnO recorded the lowest IC_{50} value against the cancer cell lines (A549 65 ± 1.02, SkBr3 53 ± 1.04 μg/ml). Likewise, 0.01-Au-ZnO (A549 115 ± 1.02, SkBr3 104 ± 1.03 μg/ml) and 0.005-Au-ZnO (A549 169 ± 1.05, SkBr3 158 ± 1.07 μg/ml) are relatively less effective. Also, against healthy HEK-293 cells, ZnO displays excellent cell viability (IC_{50} 204 ± 1.04) while it reduces with increasing the concentration of Au on ZnO (0.005 Au-ZnO 183 ± 1.07; 0.01 Au-ZnO 158 ± 1.06; 0.015 Au-ZnO 124 ± 1.01 μg/mL). Thus, the Au-ZnO nanozyme, has a dynamic dose-dependent cytotoxic effect, where 0.015-Au-ZnO is particularly potent against SkBr3 breast cancer cells while relatively low against healthy HEK293 cells.

2.9. Induction of apoptosis – acridine orange-ethidium bromide (AO-EB) dual staining

As shown in Fig. 8, the AO-EB dual staining images correspond to A549 and SkBr3 cancer cell lines. The MTT assay clearly shows the cytotoxic effect of ZnO and Au-ZnO nanocomposites against A549 and SkBr3 malignant cells. In general, cancer treatment emphasizes the induction of apoptosis, therefore detailed knowledge of cell death mechanisms is essential. Liu et al. qualitatively distinguished early and late apoptotic and necrotic cells using the AO-EB dual staining method [42]. Herein, the difference in membrane permeability of AO and EB dyes (AO permeates the membrane of normal and early apoptotic cells while EB permeates the damaged membrane of late apoptotic and dead cells) has been highly exploited. As both AO and EB dyes bind effectively with nucleic acids, they show characteristics of green (normal or early apoptotic cells) or bright orange emission (late apoptotic or necrotic cells). Cell shrinkage, nuclear and cytoplasmic condensation, chromatin fragmentation, and phagocytosis are the major characteristic features of apoptosis [76]. The control (i.e. untreated) cells are significantly larger and smoother than the ZnO and Au-ZnO treated malignant cells. The shrinkage of cell volume, rounding of cells, and fragmented and condensed chromatin formation are visible in both 0.01-Au-ZnO and 0.015-Au-ZnO treated cancerous cells. Additionally, the bright orange nucleus formation confirms that cell death occurs through an apoptotic pathway (Fig. 8).

2.10. DCFH-DA staining for ROS determination

Several cellular oxidative mechanisms generate ROS, which modulates various cellular functions and cell signalling molecules [34–39]. However, ROS at higher concentrations affects many physiological processes [44,77]. Thus, cancer cells are always associated with excess ROS production relative to normal viable cells. Therefore, it becomes essential to quantify the *in situ* generated total intracellular ROS level. For which DCFH-DA staining (2′,7′-dichlorodihydrofluorescein diacetate) was performed [43]. Herein, the presence of esterase inside the cell initiates the hydrolysis of DCFH-DA and forms non-fluorescent DCFH, which subsequently becomes green fluorescent dichlorofluorescein (DCF) by reacting with intracellular ROS. Fig. 9A shows the DCFH-DA staining images of A549 and SkBr3 carcinoma cells in the presence of ZnO, 0.005-Au-ZnO, 0.01-Au-ZnO and 0.015-Au-ZnO. The treated cancerous cells alone fluoresce green and the plate reader assay of SkBr3 cells shows high fluorescent intensity with 0.015-Au-ZnO owing to high ROS generation (Fig. 9). It acts on the tumour environment to reduce the development of tumour mass and eventually reduce the rate of tumour progression. The excess ROS level leads to severe oxidative stress, which in turn provokes apoptotic pathways responsible for mitochondrial membrane potential (MMP) loss and eventually become an effective antagonist against cancerous cells [77,78].

Table 2
In vitro cytotoxic studies of the ZnO and Au-ZnO under blue-LED illumination

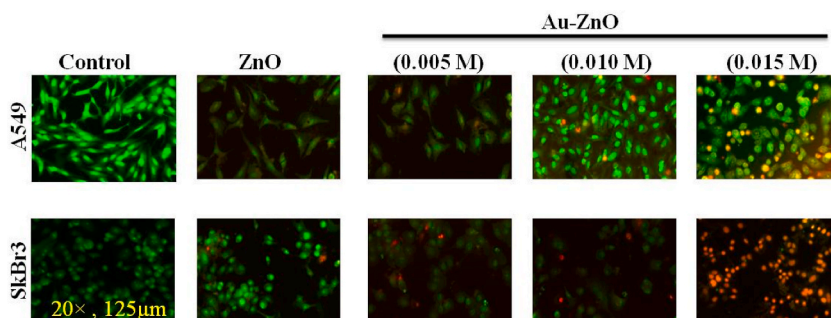| Nano-composites	A549 (μg/mL)	SkBr3 (μg/mL)	HEK-293 (μg/mL)
ZnO	174 ± 1.02	183 ± 1.08	204 ± 1.04
0.005-Au-ZnO	169 ± 1.05	158 ± 1.07	183 ± 1.07
0.01-Au-ZnO	115 ± 1.02	104 ± 1.03	158 ± 1.06
0.015-Au-ZnO	65 ± 1.02	53 ± 1.04	124 ± 1.01

Fig. 8. Morphological observation of A549 and SkBr3 cancer cell lines with AO-EB dual staining image by fluorescence microscope. Control; ZnO; 0.005M Au-ZnO; 0.010M Au-ZnO; 0.015M Au-ZnO.
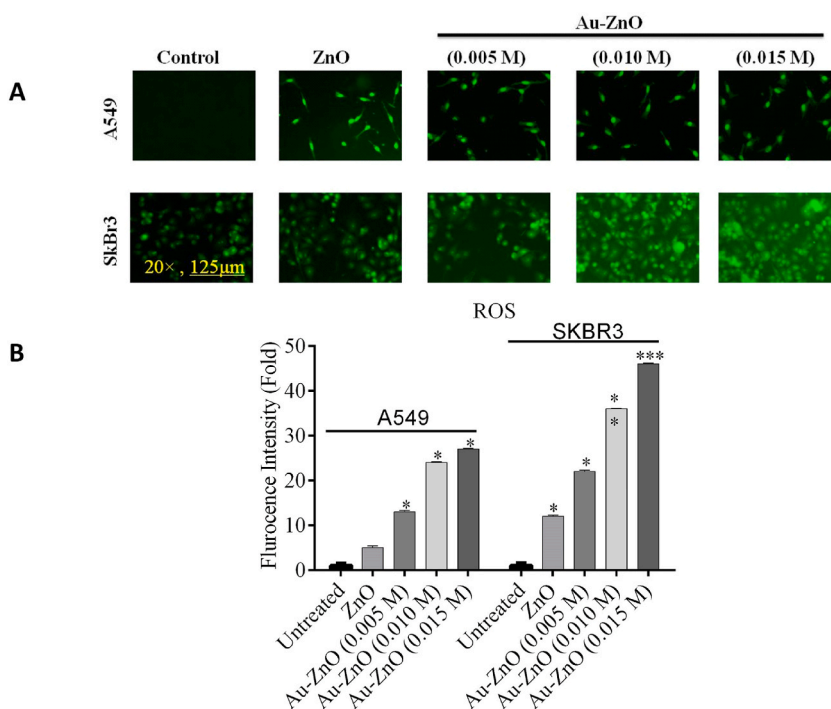

Fig. 9. A) ROS images for A549 & SkBr3 cell lines using DCFH-DA staining method from Control, ZnO, 0.005-Au-ZnO, 0.010-Au-ZnO, and 0.015-Au-ZnO. B) Quantification of the ROS level by the plate reader assay.

2.11. Plasmid cleavage ability of ZnO and Au-ZnO nanocomposites

The plasmid cleavage ability of ZnO and Au-ZnO nanocomposites was examined using the standard gel electrophoresis technique [78,79]. The conversion of supercoiled circular conformation (Form I) of PBR 322 DNA to nicked circular conformation (Form II) and linear conformation (Form III) will be monitored, and the results are depicted in Fig. 10. Au-ZnO at all tested concentrations under blue-LED illumination shows nuclease activity. The control studies based on pBR322 plasmid DNA alone showed no DNA cleavage activity (Lane 1). The supercoiled plasmid DNA was converted into circular form at 100 µg/mL. On the other hand, a higher concentration (250 µg/mL) demonstrated the conversion of form I into form III without passing through the nicked form II. We thus concluded that Au-ZnO could act as a potential chemical nuclease for double-strand DNA cleavage. This also indicates that Au-ZnO could be used as a DNA-targeting anti-cancer agent. Earlier, Zhou *et* al. showed that the TiO$_2$ may act as a nanozyme to mimic photolyase in repairing DNA damage [80].

Overall, the anticancer studies under blue LED light illumination reveal that the synthesized Au-ZnO nanocomposites actively penetrate the cell membrane and induce mitochondrial membrane potential loss (MMP). As a result of the *in situ* generation of ROS species on the Au-ZnO nanocomposite, intracellular ROS production is further triggered. Accumulation of the same in the cell cytoplasm provokes mitochondrial apoptosis followed by nuclear membrane potential loss. Consequently, it leads to DNA instability and
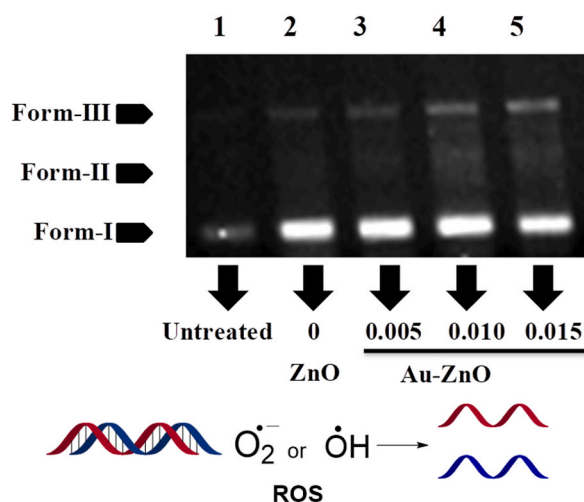
Fig. 10. Lane 1, pBR 322 DNA; Lane 2, pBR 322 DNA + ZnO 100 μg/mL; Lane 3, pBR 322 DNA +100 μg/mL Au-ZnO NPs; Lane 4, pBR 322 DNA +100 μg/mL Au-ZnO NPs; Lane 5, pBR 322 DNA +100 μg/mL Au-ZnO NPs. Incubation time 45 min.
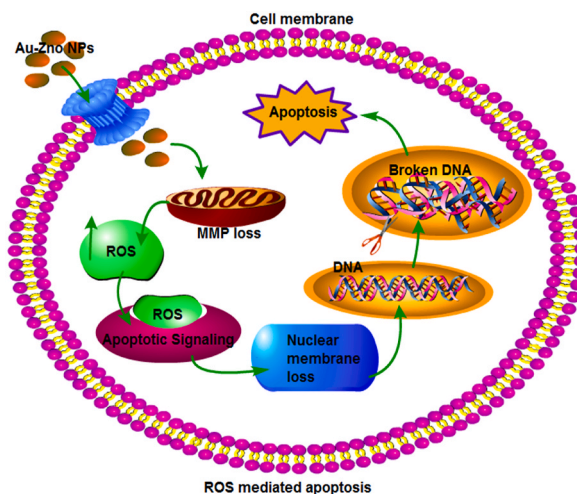

Fig. 11. Schematic representation of ROS mediated cellular apoptosis in cancer cells.

produces denatured DNA in the pBR322 plasmid (Fig. 11).

3. Conclusions

It is a well-known fact that photoactivated PMMOs generate energetic charge carriers and reactive oxygen species ($\cdot$OH and O_2^- radicals) that are essential for environmental remediation applications. Thus, we have demonstrated the use of ZnO and various concentrations of Au-ZnO (0.005, 0.01and 0.015M) against rhodamine 6G (R6G) dye degradation. Among which the 0.015-Au-ZnO shows excellent photocatalytic activity and rapid R6G degradation occurs within 15 min. Based on MTT assay, 0.015-Au-ZnO exhibits high anticancer activity against both A549 and SkBr3 cancerous cells with cell-line-specific potency towards SkBr3. AO-EB dual staining confirms early and later-stage apoptotic cell formation. The DCFH-DA analysis quantifies the intracellular ROS generation and DNA cleavage studies against pBR322 plasmid reveals that the supercoiled plasmid (form I) becomes linear single-stranded DNA (form III) without going to the nicked circular form II and leads to complete denaturation of DNA. All these observations indicating that the mitochondrial apoptosis is the plausible cell death mechanism of the cancerous cell. It is possible that the Au-ZnO nanocomposite may be a potential phototheranostic agent combined with the ability to act as a DNA-targeting anticancer agent.

Associated content
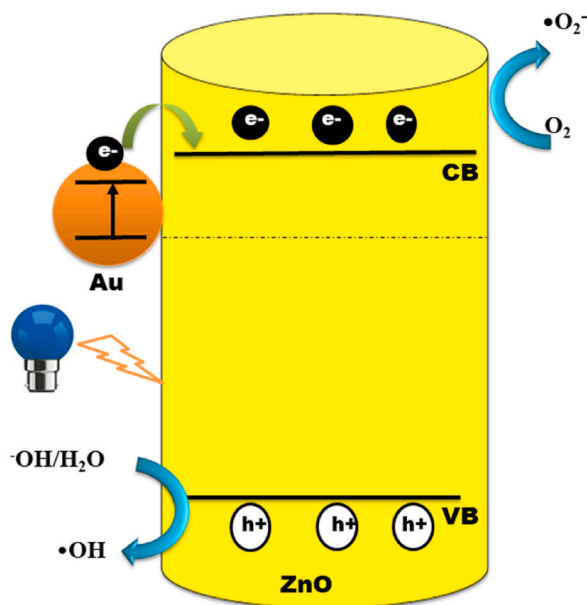
Supporting Information is available free of charge.

Fig. 12. Proposed photocatalytic mechanism of Au-ZnO under visible light irradiation [15].
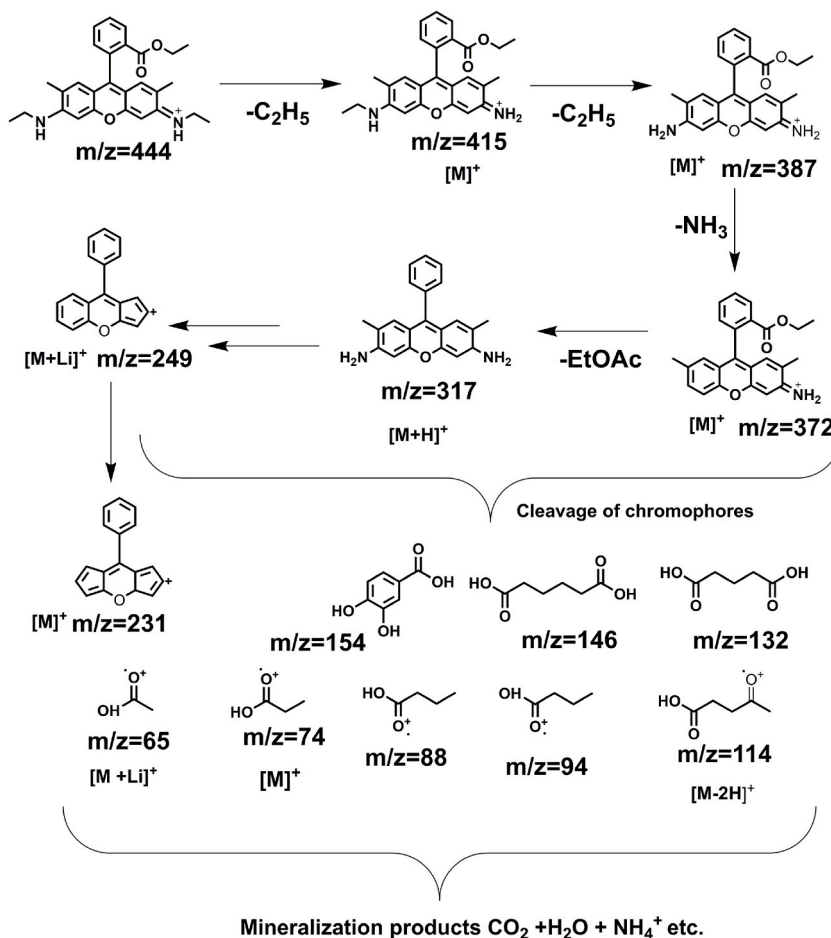

Fig. 13. LC-MS analysis of the various R6G degradation products with the plausible intermediates.

CRediT authorship contribution statement

Pilavadi Thangamuniyandi: Writing – review & editing, Writing – original draft, Validation, Methodology, Formal analysis, Data curation, Conceptualization. **Devan Umapathy:** Writing – original draft, Validation, Methodology, Investigation, Formal analysis, Data curation. **Loganathan Nagarajan:** Writing – review & editing, Writing – original draft, Validation, Supervision, Resources, Project administration, Funding acquisition, Conceptualization. **Antony Joseph Velanganni Arockiam:** Writing – original draft, Validation, Resources, Data curation.

Notes

The Authors declare no competing financial interest.

Declaration of competing interest

The authors declare that they have no known competing financial interests or personal relationships that could have appeared to influence the work reported in this paper.

Acknowledgment

Appendix A. Supplementary data

Supplementary data to this article can be found online at https://doi.org/10.1016/j.heliyon.2024.e41061.

References

[1] L. Keerthana, R. Ramyapriya, L. Elango, Geogenic and anthropogenic contamination in river water and groundwater of the lower Cauvery Basin, India, Front. Environ. Sci. 11 (2023), https://doi.org/10.3389/fenvs.2023.1001052.

[2] WHO report on Drinking Water Mar 2022. https://www.who.int/news-room/factsheets/detail/drinking-water.

[3] UNICEF data, Monitoring the situation of children and women, State of the World's drinking water (Oct 2022). https://data.unicef.org/resources/state-of-the-worlds-drinking-water/.

[4] C. von Sonntag, Advanced oxidation processes: mechanistic aspects, Water Sci. Technol. 58 (2008) 1015–1021, https://doi.org/10.2166/wst.2008.467.

[5] M.A. Oturan, J.-J. Aaron, Advanced oxidation processes in water/wastewater treatment: principles and applications. A review, Crit. Rev. Environ. Sci. Technol. 44 (2014) 2577–2641, https://doi.org/10.1080/10643389.2013.829765.

[6] S. Zahmatkesh, K.T.T. Amesho, M. Sillanpaa, A critical review on diverse technologies for advanced wastewater treatment during SARS-CoV-2 pandemic: what do we know? J. Hazard. Mater. Adv. 7 (2022) 100121 https://doi.org/10.1016/j.hazadv.2022.100121.

[7] P. Mahbub, M. Duke, Scalability of advanced oxidation processes (AOPs) in industrial applications: a review, J. Environ. Manag. 345 (2023) 118861, https://doi.org/10.1016/j.jenvman.2023.118861.

[8] M. Cheng, G. Zeng, D. Huang, C. Lai, P. Xu, C. Zhang, Y. Liu, Hydroxyl radicals based advanced oxidation processes (AOPs) for remediation of soils contaminated with organic compounds: a review, Chem. Eng. J. 284 (2016) 582–598, https://doi.org/10.1016/j.cej.2015.09.001.

[9] M.R. Hoffmann, S.T. Martin, W. Choi, D.W. Bahnemann, Environmental applications of semiconductor photocatalysis, Chem. Rev. 95 (1995) 69–96, https://doi.org/10.1021/cr00033a004.

[10] M.A. Rauf, S.S. Ashraf, Fundamental principles and applications of heterogenous photocatalytic degradation of dyes in solution, Chem. Eng. J. 151 (2009) 10–18, https://doi.org/10.1016/j.cej.2009.02.026.

[11] C. Byrne, G. Subramanian, S.C. Pillai, Recent advances in photocatalysis for environmental applications, J. Environ. Chem. Eng. 6 (2018) 3531–3555, https://doi.org/10.1016/j.jece.2017.07.080.

[12] X. Yang, D. Wang, Photocatalysis: from Fundamental principles to materials and applications, ACS Appl. Energy Mater. 1 (2018) 6657–6693, https://doi.org/10.1021/acsaem.8b01345.

[13] R. Daghrir, P. Drogui, D. Robert, Modified TiO$_2$ for environmental photocatalytic applications, A Review Ind. Eng. Chem. Res. 52 (2013) 3581–3599, https://doi.org/10.1021/ie303468t.

[14] S.G. Kumar, K.S.R.K. Rao, Zinc oxide based photocatalysis: tailoring surface-bulk structure and related interfacial charge carrier dynamics for better environmental applications, RSC Adv. 5 (2015) 3306–3351, https://doi.org/10.1039/C4RA13299H.

[15] S. Raha, Ahmaruzzaman. ZnO nanostructured materials and their potential applications: progress, challenges and perspectives, Nanoscale Adv. 4 (2022) 1868–1925, https://doi.org/10.1039/D1NA00880C.

[16] P. Wang, B. Huang, Y. Dai, M.H. Whangbo, Plasmonic photocatalysts: Harvesting visible light with noble metal nanoparticles, Phys. Chem. Chem. Phys. 14 (2012) 9813–9825, https://doi.org/10.1039/c2cp40823f.

[17] A. Rezaeifard, M. Rezaei, N. Keikha, M. Jafarpour, P. Chen, H. Jiang, Enhanced visible-light-induced photocatalytic activity in M(III)Salophen-Decorated TiO$_2$ nanoparticles for heterogeneous degradation of organic dyes, ACS Omega 8 (2023) 3821–3834, https://doi.org/10.1021/acsomega.2c05971.

[18] R.T. Tung, The physics and chemistry of the Schottky barrier height, Appl. Phys. Rev. 1 (2014) 011304, https://doi.org/10.1063/1.4858400.

[19] M.S. Arshad, Š. Trafela, K.Ž. Rožman, J. Kovač, P. Djinović, A. Pintar, Determination of Schottky barrier height and enhanced photoelectron generation in novel plasmonic immobilized multisegmented (Au/TiO$_2$) nanorod arrays (NRAs) suitable for solar energy conversion applications, J. Mater. Chem. C 5 (2017) 10509–10516, https://doi.org/10.1039/c7tc02633a.

[20] R. Kavitha, S.G. Kumar, A review on plasmonic Au-ZnO heterojunction photocatalysts: preparation, modifications and related charge carrier dynamics, Mater Sci Semicond. Proc 93 (2019) 59–91, https://doi.org/10.1016/j.mssp.2018.12.026.

[21] S. Lv, Y. Du, F. Wu, Y. Cai, T. Zhou, Review on LSPR assisted photocatalysis: effect of physical fields and opportunities in multifield decoupling, Nanoscale Adv. 4 (2022) 2608–2631, https://doi.org/10.1039/D2NA00140C.

[22] X. Chen, Y. Chen, M. Yan, M. Qiu, Nanosecond photothermal effects in plasmonic nanostructures, ACS Nano 6 (2012) 2550–2557, https://doi.org/10.1021/nn2050032.

[23] P. Christopher, H. Xin, S. Linic, Visible-light-enhanced catalytic oxidation reactions on plasmonic silver nanostructures, Nature Chem 3 (2011) 467–472, https://doi.org/10.1038/nchem.1032.

[24] A. Kudo, Y. Miseki, Heterogeneous photocatalyst materials for water splitting, Chem. Soc. Rev. 38 (2009) 253–278, https://doi.org/10.1039/B800489G.

[25] X. Liu, J. Iocozzia, Y. Wang, X. Cui, Y. Chen, S. Zhao, Z. Li, Z. Lin, Noble metal–metal oxide nanohybrids with tailored nanostructures for efficient solar energy conversion, photocatalysis and environmental remediation, Energy Environ. Sci. 10 (2017) 402–434, https://doi.org/10.1039/C6EE02265K.

[26] M.K. Choudhary, J. Kataria, S. Sharma, Novel green Biomimetic approach for preparation of highly stable Au-ZnO Heterojunctions with enhanced photocatalytic activity, ACS Appl. Nano Mater. 1 (2018) 1870–1878, https://doi.org/10.1021/acsanm.8b00272.

[27] R. Biswas, B. Banerjee, M. Saha, I. Ahmed, S. Mete, R.A. Patil, Y.-R. Ma, K.K. Haldar, Green approach for the Fabrication of Au/ZnO Nanoflowers: a catalytic Aspect, J. Phys. Chem. C 125 (2021) 6619–6631, https://doi.org/10.1021/acs.jpcc.0c10149.

[28] M.D.L.R. Peralta, U. Pal, R.S. Zeferino, Photoluminescence (PL) Quenching and enhanced photocatalytic activity of Au-decorated ZnO nanorods Fabricated through microwave-assisted chemical synthesis, ACS Appl. Mater. Interfaces 4 (2012) 4807–4816, https://doi.org/10.1021/am301155u.

[29] X. Li, J.F. Lovell, J. Yoon, X. Chen, Clinical development and potential of photothermal and photodynamic therapies for cancer, Nat. Rev. Clin. Oncol. 17 (2020) 657–674, https://doi.org/10.1038/s41571-020-0410-2.

[30] X. Yin, Y. Cheng, Y. Feng, W.R. Stiles, S.H. Park, H. Kang, H.S. Choi, Phototheranostics for multifunctional treatment of cancer with fluorescence imaging, Adv. Drug Deliv. Rev. 189 (2022) 114483, https://doi.org/10.1016/j.addr.2022.114483.

[31] H. Villuendas, C. Vilches, R. Quidant, Influence of cell type on the efficacy of plasmonic photothermal therapy, ACS Nanosci. Au. 2 (2022) 494–502, https://doi.org/10.1021/acsnanoscienceau.2c00023.

[32] V. Guerrero-Florez, S.C. Mendez-Sanchez, O.A. Patron-Soberano, V. Rodriguez-Gonzalez, D. Blach, F. Martinez O, Gold nanoparticle-mediated generation of reactive oxygen species during plasmonic photothermal therapy: a comparative study for different particle sizes, shapes, and surface conjugations, J. Mater. Chem. B 8 (2020) 2862–2875, https://doi.org/10.1039/D0TB00240B.

[33] O.K. Ranasingha, C. Wang, P.R. Ohodnicki, J.W. Lekse, J.P. Lewis, C. Matranga, Synthesis, characterization, and photocatalytic activity of Au-ZnO nanopyramids, J. Mater. Chem. A. 3 (2015) 15141–15147, https://doi.org/10.1039/c5ta01344e.

[34] W. He, H.K. Kim, W.G. Wamer, D. Melka, J.H. Callahan, J.J. Yin, Photogenerated charge carriers and reactive oxygen species in ZnO/Au hybrid nanostructures with enhanced photocatalytic and antibacterial activity, J. Am. Chem. Soc. 136 (2014) 750–757, https://doi.org/10.1021/ja410800y.

[35] X. Jiang, W. He, X. Zhang, Y. Wu, Q. Zhang, G. Cao, H. Zhang, J. Zheng, T.R. Croley, J.J. Yin, Light-Induced Assembly of metal nanoparticles on ZnO enhances the generation of charge carriers, reactive oxygen species, and antibacterial activity, J. Phys. Chem. C 122 (2018) 29414–29425, https://doi.org/10.1021/acs.jpcc.8b10578.

[36] A.A. Dayem, M.K. Hossain, S.B. Lee, K. Kim, S.K. Saha, G.-M. Yang, H.Y. Choi, S.-G. Cho, The role of reactive oxygen species (ROS) in the biological activities of metallic nanoparticles, Int. J. Mol. Sci. 18 (2017) 120, 10.3390%2Fijms18010120.

[37] B. Yang, Y. Chen, J. Shi, Reactive oxygen species (ROS)-Based nanomedicine, Chem Rev. 119 (2019) 4881–4985, https://doi.org/10.1021/acs.chemrev.8b00626.

[38] Y. Nosaka, A.Y. Nosaka, Generation and Detection of reactive oxygen species in photocatalysis, Chem. Rev. 117 (2017) 11302–11336, https://doi.org/10.1021/acs.chemrev.7b00161.

[39] Y. Hu, B.Y. Zhang, F. Haque, G. Ren, J.Z. Ou, Plasmonic metal oxides and their biological applications, Mater. Horiz. 9 (2022) 2288–2324, https://doi.org/10.1039/D2MH00263A.

[40] T. Mosmann, Rapid colorimetric assay for cellular growth and survival: application to proliferation and cytotoxicity assays, J. Immunol. Methods 65 (1983) 55–63, https://doi.org/10.1016/0022-1759(83)90303-4.

[41] N. Gerlier, N. Thomasset, Use of MTT colorimetric assay to measure cell activation, J. Immunol. Methods 94 (1986) 57–63, https://doi.org/10.1016/0022-1759(86)90215-2.

[42] K. Liu, P. cheng Liu, R. Liu, X. Wu, Dual AO/EB staining to detect apoptosis in osteosarcoma cells compared with flow cytometry, Med. Sci. Monit. Basic Res. 21 (2015) 15–20, https://doi.org/10.12659/MSMBR.893327.

[43] A. Aranda, L. Sequedo, L. Tolosa, G. Quintas, E. Burello, J. V Castell, L. Gombau, Dichloro-dihydro-fluorescein diacetate (DCFH-DA) assay: a quantitative method for oxidative stress assessment of nanoparticle-treated cells, Toxicol. Vitr. 27 (2013) 954–963, https://doi.org/10.1016/j.tiv.2013.01.016.

[44] M.S. Cooke, M.D. Evans, M. Dizdaroglu, J. Lunec, Oxidative DNA damage: mechanisms, mutation, and disease, FASEB J 17 (2003) 1195–1214, https://doi.org/10.1096/fj.02-0752rev.

[45] V. Sharma, Sol-gel mediated facile synthesis of zinc-oxide nanoaggregates, their characterization and antibacterial activity, J. Appl. Chem. 2 (2012) 52–55, https://doi.org/10.9790/5736-0265255.

[46] J. Kimling, M. Maier, B. Okenve, V. Kotaidis, H. Ballot, A. Plech, Turkevich method for gold nanoparticle synthesis Revisited, J. Phys. Chem. B 110 (2006) 15700–15707, https://doi.org/10.1021/jp061667w.

[47] J. F. Moulder, W. F. Stickle, P. E. Sobol, K. D. Bomben, Handbook of X-Ray Photoelectron Spectroscopy 1995, ULVAC-PHI, Inc., Japan.

[48] F.A. Stevie, C.L. Donley, Introduction to x-ray photoelectron spectroscopy, J. Vac. Sci. Technol. A 38 (2020) 063204, https://doi.org/10.1116/6.0000412.

[49] O. Al Rugaie, M.S. Jabir, M.K. Mohammed, R.H. Abbas, D.S. Ahmed, G.M. Sulaiman, H.A. Mohammed, Modification of SWCNTs with hybrid materials ZnO-Ag and ZnO-Au for enhancing bactericidal activity of phagocytic cells against Escherichia coli through NOX2 pathway, Sci. Rep. 12 (2022) 17203, https://doi.org/10.1038/s41598-022-22193-1.

[50] P. Fageria, S. Gangopadhyay, S. Pande, Synthesis of ZnO/Au and ZnO/Ag nanoparticles and their photocatalytic application using UV and visible light, RSC Adv. 4 (2014) 24962–24972, https://doi.org/10.1039/c4ra03158j.

[51] C. Mondal, J. Pal, M. Ganguly, A.K. Sinha, J. Jana, T. Pal, A one pot synthesis of Au-ZnO nanocomposites for plasmon-enhanced sunlight driven photocatalytic activity, New J. Chem. 38 (2014) 2999–3005, https://doi.org/10.1039/c4nj00227j.

[52] S. Yang, L. Wang, Y. Yan, L. Yang, X. Li, Z. Lu, H. Zhai, D. Han, P. Huo, Two hybrid Au ZnO Heterostructures with different Hierarchical structures: towards highly efficient photocatalysts, Sci. Rep. 9 (2019) 1–10, https://doi.org/10.1038/s41598-019-53212-3.

[53] S. Verma, B.T. Rao, R. Singh, R. Kaul, Photocatalytic degradation kinetics of cationic and anionic dyes using Au-ZnO nanorods: role of pH for selective and simultaneous degradation of binary dye mixture, Ceram. Inter. 47 (2021) 34751–34764, https://doi.org/10.1016/j.ceramint.2021.09.014.

[54] M.P. Casaletto, A. Lango, A. Martorana, A. Prestianni, A.M. Venizia, XPS study of supported gold catalysts: the role of Au^0 and $Au^{+\delta}$ species as active sites, Surf. Interface Anal. 38 (2006) 215–218, https://doi.org/10.1002/sia.2180.

[55] L. Wolski, I. Sobczak, M. Ziolek, Variability of surface components in gold catalysts – the role of hydroxyls and state of gold on activity and selectivity of Au-Nb_2O_5 and Au-$ZnNb_2O_6$ in methanol oxidation, J. Catal. 354 (2017) 100–112, https://doi.org/10.1016/j.jcat.2017.08.022.

[56] L. Wolski, A. Wolkowiak, M. Ziolek, Formation of reactive oxygen species upon interaction of Au/ZnO with H_2O_2 and their activity in methylene blue degradation, Catal. Today 333 (2019) 54–62, https://doi.org/10.1016/j.cattod.2018.04.004.

[57] X. Sun, L. Zhu, Y. Zhang, M. Li, Y. Wang, C. Qin, Y. Wang, Simulated sunlight enhanced methane-sensing performance based on Au-modified ZnO microsphere under room temperature, J. Mater. Sci. Mater. Electron. 34 (2023) 1950–1962, https://doi.org/10.1007/s10854-023-11313-w.

[58] T.J. Frankcombe, Y. Liu, Interpretation of oxygen 1s X-ray photoelectron spectroscopy of ZnO, Chem. Mater. 35 (2023) 5468–5474, https://doi.org/10.1021/acs.chemmater.3c00801.

[59] H. Zhang, D. Yang, Y. Ji, X. Ma, J. Xu, D. Que, Low temperature synthesis of Flowerlike ZnO nanostructures by Cetyltrimethylammonium bromide-assisted hydrothermal process, J. Phys. Chem. B 108 (2004) 3955–3958, https://doi.org/10.1021/jp036826f.

[60] V. Ischenko, S. Polarz, D. Grote, V. Stavarache, K. Fink, M. Driess, Zinc oxide nanoparticles with defects, Adv. Funct. Mater. 15 (2005) 1945–1954, https://doi.org/10.1002/adfm.200500087.

[61] S.A. Ansari, M.M. Khan, S. Kalathil, A. Nisar, J. Lee, M.H. Cho, Oxygen vacancy induced band gap narrowing of ZnO nanostructures by an electrochemically active biofilm, Nanoscale 5 (2013) 9238–9246, https://doi.org/10.1039/c3nr02678g.

[62] S. Thaler, C. Haritoglou, T.J. Choragiewicz, A. Messias, A. Baryluk, C.A. May, R. Rejdak, M. Fiedorowicz, E. Zrenner, F. Schuettauf, In vivo Toxicity study of rhodamine 6G in the rat Retina, Investig. Ophthalmol. Vis. Sci. 49 (2008) 2120–2126, https://doi.org/10.1167/iovs.07-1476.

[63] F.M. Zehentbauer, C. Moretto, R. Stephen, T. Thevar, J.R. Gilchrist, D. Pokrajac, K.L. Richard, J. Kiefer, Fluorescence spectroscopy of Rhodamine 6G: concentration and solvent effects, Spectrochim. Acta Mol. Biomol. Spectrosc. 121 (2014) 147–151, https://doi.org/10.1016/j.saa.2013.10.062.

[64] M.E. Aguirre, A. Armanelli, G. Perelstein, A. Feldhoff, A.J. Tolley, M.A. Grela, Modulation of the electron transfer processes in Au–ZnO nanostructures, Nanoscale 7 (2015) 6667–6674, https://doi.org/10.1039/C5NR00364D.

[65] T.S. Natarajan, M. Thomas, K. Natarajan, H.C. Bajaj, R.J. Tayade, Study on UV-LED/TiO2 process for degradation of Rhodamine B dye, Chem. Eng. J. 169 (2011) 126–134, https://doi.org/10.1016/j.cej.2011.02.066.

[66] S. Rasalingam, R. Peng, R.T. Koodali, An insight into the adsorption and photocatalytic degradation of rhodamine B in periodic mesoporous materials, Appl. Catal. B Environ. 174–175 (2015) 49–59, https://doi.org/10.1016/j.apcatb.2015.02.040.

[67] T. Rasheed, M. Bilal, H.M.N. Iqbal, H. Hu, X. Zhang, Reaction mechanism and degradation pathway of rhodamine 6G by photocatalytic treatment, Water, Air, Soil Pollut 228 (2017) 291, https://doi.org/10.1007/s11270-017-3458-6.

[68] M.P. Vinardell, M. Mitjans, Antitumour activities of metal oxide nanoparticles, Nanomaterials 5 (2015) 1004–1021, https://doi.org/10.3390/nano5021004.

[69] D. Hariharan, P. Thangamuniyandi, A. Jegatha Christy, R. Vasantharaja, P. Selvakumar, S. Sagadevan, A. Pugazhendhi, L.C. Nehru, Enhanced photocatalysis and anticancer activity of green hydrothermal synthesized Ag@TiO2 nanoparticles, J. Photochem. Photobiol. B Biol. 202 (2020) 111636, https://doi.org/10.1016/j.jphotobiol.2019.111636.

[70] M.J. Akhtar, M. Ahamed, S. Kumar, M.A.M. Khan, J. Ahmad, S.A. Alrokayan, Zinc oxide nanoparticles selectively induce apoptosis in human cancer cells through reactive oxygen species, Int. J. Nanomedicine 7 (2012) 845–857, https://doi.org/10.2147/IJN.S29129.

[71] G. Bisht, S. Rayamajhi, ZnO nanoparticles as promising anticancer agents, Nanobiomedicine 3 (2016), https://doi.org/10.5772/63437.

[72] M. Pandurangan, G. Enktaivan, D.H. Kim, Anticancer studies of synthesized ZnO nanoparticles against human cervical carcinoma cells, J. Photochem. Photobiol. B: Biology 158 (2016) 206–211, https://doi.org/10.1016/j.jphotobiol.2016.03.002.

[73] J. Bresee, C.M. Bond, R.J. Worthington, C.A. Smith, J.C. Gifford, C.A. Simpson, C.J. Carter, G. Wang, J. Hartman, N.A. Osbaugh, R.K. Shoemaker, C. Melander, D.L. Feldheim, Nanoscale structure–activity relationships, Mode of action, and Biocompatibility of gold nanoparticle Antibiotics, J. Am. Chem. Soc. 136 (2014) 5295–5300, https://doi.org/10.1021/ja408505n.

[74] S. Anjum, M. Hashim, S.A. Malik, M. Khan, J.M. Lorenzo, B.H. Abbasi, C. Hano, Recent advances in zinc oxide nanoparticles (ZnO NPs) for cancer Diagnosis, Target drug Delivery, and treatment, Cancers 13 (2021) 4570, https://doi.org/10.3390/cancers13184570.

[75] R.J. Kadhim, E.H. Karsh, Z.J. Taqi, M.S. Jabir, Biocompatibility of gold nanoparticles: in-vitro and In-vivo study, Mater. Today Proc. 42 (2021) 3041–3045, https://doi.org/10.1016/j.matpr.2020.12.826.

[76] A. Saraste, K. Pulkki, Morphologic and biochemical hallmarks of apoptosis, Cardiovasc. Res. 45 (2000) 528–537, https://doi.org/10.1016/s0008-6363(99)00384-3.

[77] L.B. Sullivan, N.S. Chandel, Mitochondrial reactive oxygen species and cancer, Cancer Metabol. 2 (2014) 17–28, https://doi.org/10.1186/2049-3002-2-17.

[78] S. Khan, W.C. Cho, L.A. Jaragh-Alhadad, R. Tarharoudi, S.H. Bloukh, Z. Edis, S. Sari, M. Falahati, T.L.M. ten Hagen, R.H. Khan, Q. Bai, Nano-bio interaction: an overview on the biochemical binding of DNA to inorganic nanoparticles for the development of anticancer and antibacterial nano-platforms, Int. J. Biol. Macromol. 225 (2023) 544–556, https://doi.org/10.1016/j.ijbiomac.2022.11.110.

[79] A. De, R. Das, H. Kaur, P. Jain, Synthesis, physicochemical investigations, DNA cleavage activity of biogenic zinc oxide nanoparticles and their interaction with Calf-Thymus DNA, Mater. Today Proc. 49 (2022) 3260–3264, https://doi.org/10.1016/j.matpr.2020.12.742.

[80] Q. Zhou, T. Zhang, J. Jie, Y. Hou, Z. Hu, Z. Jiao, H. Su, TiO2 as a nanozyme Mimicking photolyase to Repair DNA damage, J. Phys. Chem. Lett. 13 (2022) 10929–10935, https://doi.org/10.1021/acs.jpclett.2c02717.